

Electrically Programmable Pixelated Graphene-Integrated Plasmonic Metasurfaces for Coherent Mid-Infrared Emission

Xiu Liu^{1,†}, Yibai Zhong^{1,†}, Zexiao Wang¹, Tianyi Huang¹, Sen Lin², Jingyi Zou², Haozhe Wang⁴, Zhien Wang⁴, Zhuo Li¹, Xiao Luo¹, Rui Cheng¹, Jiayu Li¹, Hyeong Seok Yun¹, Han Wang³, Jing Kong⁴, Xu Zhang^{2,*}, Sheng Shen^{1,*}

¹Department of Mechanical Engineering, Carnegie Mellon University, Pittsburgh, PA, USA

²Department of Electrical and Computer Engineering, Carnegie Mellon University, Pittsburgh, PA, USA

³Department of Electrical and Electronic Engineering, University of Hong Kong, Hong Kong, China

⁴Department of Electrical Engineering and Computer Science, Massachusetts Institute of Technology, Cambridge, MA, USA

(† denotes equal contribution, * denotes corresponding authors)

Abstract

Active metasurfaces have recently emerged as compact, lightweight, and efficient platforms for dynamic control of electromagnetic fields and optical responses. However, the complexities associated with their post-fabrication tunability significantly hinder their widespread applications, especially for the mid-infrared range due to material scarcity and design intricacy. Here, we experimentally demonstrate highly dynamic, pixelated modulations of coherent mid-infrared emission based on an electrically programmable plasmonic metasurface integrated with graphene field effect transistors (Gr-FETs). The ultrabroad infrared transparency of graphene allows for free-form control over plasmonic meta-atoms, thus achieving coherent mid-infrared states across a broad range of wavelengths and polarizations. The spatial temperature modulation generated by Gr-FETs is effectively synergized with the emissivity control by the localized surface plasmon polaritons from gold nanoantennas. This integrated temperature-emissivity modulation of metasurfaces is systematically extended to form a pixelated 2D array, envisioning new approaches toward scalable 2D electrical wiring for densely packed, independently controlled pixels.

Introduction

Active metasurfaces, which consist of planar arrays of subwavelength light scatters or antennas (“meta-atoms”), enable dynamic and versatile control over electromagnetic field states and optical responses^{1,2}. Compared to conventional bulk optics, they feature ultra-compact, lightweight, and energy-efficient systems, which are particularly promising for applications constrained by a lean size, weight, or power budget, such as aerospace remote sensing, free-space communication, and point-of-care and wearable health monitoring³⁻⁵. The high-density meta-atoms capitalizing great amounts of degrees of freedom also facilitate real-time beam shaping and steering for devices including light detection and ranging (LiDAR) in autonomous vehicles and light-field display in augmented/virtual reality (AR/VR) modules⁶⁻¹⁰. However, compared with their passive counterparts, the extra complexity for post-fabrication tunability introduced in active metasurfaces poses notable technical challenges for implementing these advanced functions^{2,11}, particularly in the mid-infrared regime due to the dearth of rational materials and device designs. For instance, subwavelength-scaled arrays of narrow-bandgap semiconductors suffer from costly crystal growth and require external cooling, impeding the miniaturized device integration^{12,13}. The dynamic switching of phase-change metasurfaces is typically limited to a dichotomy between metallic and dielectric states¹⁴⁻¹⁶, while multistate phase transition encounters a narrow working window to attain critical temperatures¹⁷.

Recent advances in thermal photonics reveal a new route for achieving dynamic light control in the mid-infrared range¹⁸⁻²². The metasurface-augmented polaritonic and photonic modes, including surface plasmon polaritons from plasmonic metals^{23,24}, surface phonon polaritons from polar dielectrics²⁵⁻²⁷, photonic crystals and their twisted bilayers^{28,29}, show strong temporal, spatial, or polarized coherence (i.e., narrowband, directional, or polarized emission). These modes can be unified to engineer the photonic density of states DOS for the thermal infrared emission intensity formulated as

$$I = E(\omega, T) \cdot DOS(\omega, \hat{n}, \hat{p}) \quad (1)$$

where ω is the frequency, E is the average energy per photon $\hbar\omega/(e^{\hbar\omega/k_B T} - 1)$ at temperature T , \hat{n} is the normal vector of direction, and \hat{p} is the polarization vector¹⁸⁻²⁰. Based on Eq. (1), one can identify two modulation schemes: the first involves the average photon energy E , which can be controlled by temperature T , whereas the second pertains to the photonic density of states DOS ,

which corresponds to emissivity, a far-field term normalized to an ideal blackbody commonly employed in radiometry.

To date, various methods have been employed to actively excite thermal infrared metasurfaces, such as thermal hot plate^{30,31}, mechanical actuation³², and optical laser pulse³³. However, the realization of electrically programmable on-chip integration for large-area pixelated 2D arrays remains a significant challenge. Single-pixel active metasurfaces, by electrically modulated refractive indices of materials like graphene^{34–38} and transparent conductive oxides (indium silicon oxide³⁹, indium tin oxide^{40,41}), typically yields limited infrared emissivity contrast. Joule heating in an incandescent metasurface with a fixed resistance restricts the pixel modulation to binary on/off states and imposes constraints on the available design parameters for coherent characteristics due to the overlap of electrodes with optically active regions^{42–44}. Although state-of-the-art research has predominantly featured in-plane fan-out writing designs for 1D arrays^{6,7,45–47}, electrically driven 2D pixelated metasurfaces have rarely been demonstrated due to the complexities of electrical addressing.

Due to the carbon nature and strong covalent bonding, graphene is stable at elevated temperatures and durable in long working cycles^{48,49}, and can function as a robust, transparent, high-speed, and tunable microheater. The atomically thin single-layer graphene makes it as a broadband transparent electrode from visible to far-infrared^{50,51}, whose time constant for Joule heating can reach picoseconds^{52,53}. More importantly, the semi-metallic nature of graphene allows a fine-tuning of its carrier density by electrostatic gating, allowing for tunable microscale localized heating^{54–56}. Based on this spatial temperature modulation, we develop an integrated emissivity-temperature scheme to create an electrically programmable 2D-pixelated mid-infrared metasurface, where emissivity control and temperature regulation are achieved by tuning heating position and strength, respectively.

In this work, we experimentally demonstrate the pixelated modulation of coherent thermal emission from an electrical-programmable plasmonic metasurface integrated with a graphene field effect transistor (Gr-FET). The exceptionally broadband transparency of single-layer graphene enables free-form control over plasmonic meta-atoms fulfilling the design space for controlling mid-infrared coherent states across a wide range of wavelengths and polarizations. The spatial temperature modulation generated by the Gr-FET is effectively synergized with the emissivity control by the localized surface plasmon polaritons (LSPPs) from gold nanoantennas. This

integrated temperature-emissivity modulation is systematically extended to form a pixelated 2D array, signifying a new approach toward scalable 2D electrical wiring for densely packed, individually addressable pixels. Specifically, a 3×3 sweeping pixel array demonstrates diverse alphanumeric displays, supported by an explicit analytical model detailing the control mechanism. Our method offers superior potential in large-area scalability: to independently control $N \times N$ pixel arrays, only $2N + 1$ electrical pins rather than N^2 pins are required. The extremely small thermal mass from the ultrathin graphene film further enables rapid modulation, achieving a 3-dB bandwidth of 146 kHz in a total $95 \mu\text{m} \times 95 \mu\text{m}$ device. In conjunction with CMOS-compatible fabrication and outstanding high-temperature resilience of large-area graphene grown by chemical vapor deposition (CVD), our device represents a significant stride in the development of next-generation mid-infrared active metadevices.

Integrated Emissivity-Temperature Active Metasurfaces

We design and fabricate pixelated active metasurfaces electrically driven by Gr-FETs, as shown in Fig. 1(a). Each pixel consists of an array of gold (Au) plasmonic nanoantennas in direct contact with a single-layer graphene channel. The graphene layer is patterned and fabricated into Gr-FETs with source and drain contacts made of Au. Beneath lies an aluminum oxide (Al_2O_3) layer, which functions as the gate dielectric of the Gr-FET. The plasmonic nanoantennas and the Au bottom gate electrode of the Gr-FET serve as the meta-atoms and mirror of the metal-insulator-metal (MIM) metasurface, respectively. The Al_2O_3 layer is also co-optimized as the spacer of the MIM metasurface to achieve critical coupling. The Gr-FET structure provides a tunable and programmable Joule heating channel to modulate the spatial temperature distribution of metasurfaces. The source/drain and bottom gate electrodes of Gr-FETs are further patterned to allow for spatial temperature modulation in an addressable pixelated mode. In Fig. 1(b), the active pixelated metadvice is fabricated using hybrid optical and electron lithography processes (detailed design parameters and fabrication procedures in the “Method” section). The zoom-in image in Fig. 1(b) shows a typical Au nanosquares based MIM metasurface, in which the LSPP mode supports the narrowband emission at the wavelength around $2.9 \mu\text{m}$ (as depicted in Supplementary S2). The emission states can be finely tuned by engineering the geometries of the meta-atoms, as illustrated by the finite-difference time-domain (FDTD) simulations. As shown in

Fig. 1(c), the resonance wavelength can be tuned across a range of 2.9 μm to 4.8 μm as the side length of nanosquares changes from 500 nm to 750 nm.

As described in Eq. (1), thermal emission of a metasurface is generally controlled by its emissivity and local temperature. Here, by integrating pixelated plasmonic metasurfaces with Gr-FETs, we introduce an integrated emissivity-temperature scheme to actively modulate coherent thermal emission from metasurfaces in the mid-infrared range. Specifically, the Gr-FETs precisely shift the heating position to the target pixel metasurface with a designated emissivity. Other than the size-dependent tuning of resonant wavelength in Fig. 1(c), the emissivity engineering of the free-form meta-atoms, facilitated by the graphene infrared transparency, can be further demonstrated by tuning the polarization of the Au nanorods array. Figure 2(a) illustrates two pixels composed of perpendicular Au nanorods with distinct lengths fabricated directly on a single graphene channel. In Fig. 2(b), their measured length-dependent resonant spectra depict one emission peak at 3.9 μm along polarization angle $\theta = 0^\circ$ (blue curve) and the other at 5.3 μm along $\theta = 90^\circ$ (red curve). As shown by the polar plot in Fig. 2(c), the emission peaks of the two pixels are measured across a range of polarization angles from 0° to 180° , where two orthogonal polarization states are clearly observed. The direct contact between the Au nanoantennas and graphene also enables tunable emissivity directly through an electrostatic gating (instead of switching the heating position) on the active metasurface, where the gating-induced carrier doping in graphene alters the dielectric environment for the LSPPs from the Au nanoantennas. However, due to the limited carrier mobility of the CVD graphene, the resonance peak of the metasurface only undergoes a $\sim 0.5 \mu\text{m}$ blue shift from a gate voltage reaching the Dirac point of the graphene to considerably far from the Dirac point (Supplementary S3), which is consistent with previous studies^{34–38}.

The Gr-FETs allow for programmable spatial temperature modulation because the semi-metallic nature of graphene enables fine tuning of its carrier density and channel resistivity through electrostatic gating. In contrast with traditional metal-based heating with a fixed resistance, the graphene-based tunable heaters can be more straightforwardly scaled up to a large-area on-chip 2D array with densely packed, independently controlled pixels, and potentially achieve a high speed due to the near-zero thermal mass of single-layer graphene. For a Gr-FET with a sole bottom gate electrode, the Joule heating reaches its maximum and generates a “hot-spot” at the position where the local resistivity of graphene is the highest. The local resistivity $\rho(x)$ along the graphene channel can be expressed as (detailed derivations in Supplementary S1)

$$\rho(x) = \sqrt{\frac{W}{2IC_{ox}\mu}} \cdot \frac{1}{\sqrt{\text{sgn}(x - x_0) \cdot (x - x_0)}} \quad (2)$$

where W is the width of the graphene channel, I is the steady channel current and is kept as constant along the graphene channel, C_{ox} is the gate dielectric capacitance per unit area, and μ is the carrier mobility that is approximated as constant⁵⁶. x_0 is the position reaching the Dirac point, and sgn is the sign function. For the spatial temperature modulation from $x = 0$ to L , we have

$$\frac{\text{sgn}(x_0 - L)}{\text{sgn}(x_0)} \sqrt{\frac{\text{sgn}(L - x_0)(L - x_0)}{\text{sgn}(-x_0)(-x_0)}} = \frac{V_{Dirac} - V_g}{V_{Dirac} - V_g + V_d} \quad (3)$$

where V_g is the gate voltage, V_d is the drain voltage, L is the channel length, and the source electrode is grounded. V_{Dirac} is the Dirac voltage corresponding to the neutrality point of graphene depending on its intrinsic doping and substrate. Hence, the hot spot on the Gr-FET can be controlled and continuously shifted in a programmable way by tuning V_g and V_d . As shown in Fig. 3(a), a preliminary sweep of source-drain current versus gate voltage I_d - V_g is conducted for the Gr-FET under a low drain voltage $V_d = 50 \text{ mV}$ (with the source electrode grounded) to determine the Dirac voltage $V_{Dirac} = -2 \text{ V}$. Figure 3(b) shows a metadvice composed of two pixels with identical resonant emission wavelengths along the graphene channel with a total length of L . When operating under a source-drain bias of $V_d = 30 \text{ V}$, the Gr-FET is expected to show a Dirac point at the position $x_0 = 0.8L$ for $V_g = 8 \text{ V}$ as calculated by Eq. (3), and thus the lower pixel exhibits stronger thermal infrared emission, as shown in Fig. 3(c). With the same $V_d = 30 \text{ V}$, however, at $V_g = 30 \text{ V}$, the Dirac point position would lie outside the graphene channel region (i.e., $x_0 < 0$), thus resulting in a stronger illumination in the upper pixel (Fig. 3(d)). For $V_g = 16 \text{ V}$ and $V_d = 30 \text{ V}$, the Dirac point lies in the gap between two pixels, and therefore the two pixels exhibit comparable but notably weaker thermal emission (Fig. 3(e)) compared to the scenarios at $V_g = 8 \text{ V}$ and $V_g = 30 \text{ V}$ due to its larger overall resistance of the Gr-FET.

Pixelated 2D Array Dynamics with Regulated Emission

Here, we introduce addressable pixelated active metasurfaces with separated local gate electrodes for each pixel. Figure 4(a) shows an active metadvice integrated with a custom-designed printed

circuit board (PCB). In the zoom-in view in Fig. 4(b), the bottom gate electrode is distinctly partitioned into three segments, each specifically associated with one individual pixel. The control of each gate voltage is demonstrated in the sweep mapping of $I_{d2} - (V_{g1}, V_{g2})$ under $V_{d2} = 50 \text{ mV}$ in Fig. 4(c), where the gate electrode 3 is grounded (i.e., V_{g3}). For each value of the gate 1 voltage V_{g1} , the sweep of $I_{d2} - V_{g2}$ for the gate 2 maintains the bipolar transport characteristic curve of the Gr-FET (Fig. 3(a)). When V_{g2} is tuned for the V_{Dirac} alignment for the pixel on/off, V_{g1} can be set to be away from V_{Dirac} (as depicted by point A) to increase the overall current along the graphene channel for an enhanced pixel brightness. By symmetry, this strategy applies to the sweep of $I_{d2} - V_{g1}$ under the control by V_{g2} , as labeled by point B. Through this methodology, we have the capability not only to adjust the position of the heated pixel but also to regulate its heating intensity, which also indicates the pixel's brightness. The coupling between pixels can be described as 3 Gr-FETs in series whose Dirac point positions x_{01}, x_{02}, x_{03} are given by (detailed derivations in Supplementary S1)

$$\left\{ \begin{array}{l} V_{g1} - V_{g2} = -\text{sgn}\left(\frac{L}{3} - x_{02}\right) \sqrt{\text{sgn}\left(\frac{L}{3} - x_{02}\right) C\left(\frac{L}{3} - x_{02}\right)} + \text{sgn}\left(\frac{L}{3} - x_{01}\right) \sqrt{\text{sgn}\left(\frac{L}{3} - x_{01}\right) C\left(\frac{L}{3} - x_{01}\right)} \\ V_{g2} - V_{g3} = -\text{sgn}\left(\frac{2L}{3} - x_{03}\right) \sqrt{\text{sgn}\left(\frac{2L}{3} - x_{03}\right) C\left(\frac{2L}{3} - x_{03}\right)} + \text{sgn}\left(\frac{2L}{3} - x_{02}\right) \sqrt{\text{sgn}\left(\frac{2L}{3} - x_{02}\right) C\left(\frac{2L}{3} - x_{02}\right)} \\ V_{Dirac} - [V_{g1} - V_d] = -\text{sgn}(0 - x_{01}) \sqrt{\text{sgn}(0 - x_{01}) C(0 - x_{01})} \\ V_{Dirac} - [V_{g3} - 0] = -\text{sgn}(L - x_{03}) \sqrt{\text{sgn}(L - x_{03}) C(L - x_{03})} \end{array} \right. \quad (4)$$

The resistance R_i for each pixel $i = 1, 2, 3$ can then be derived by integrating the local resistivity Eq. (2) using the inputs x_{01}, x_{02}, x_{03} for each segment. At $V_{d2} = 5 \text{ V}$, Figure 4(d) employs $[V_{g1}, V_{g2}, V_{g3}] = [-2, 2, -2] \text{ V}$ to light up the central pixel with the computed resistances as $[R_1, R_2, R_3] = [529, 1877, 1023] \Omega$. The addressable pixelated operation can be readily scaled up to a large-area 2D array for real-world applications. Figure 4(e) demonstrates a 3×3 pixelated display showing letter “L” by electrically programming individual frames. Various letter or number patterns can be generated using distinct pixel sweep schemes (demonstration videos available in Supplementary Information). These display demonstrations by independent pixel control use only 7 electrical pins (total “ $2N + 1$ ” pins with 3 gate electrodes, 3 drain electrodes, and 1 grounded source electrode), fewer than 9 pins (corresponding to “ N^2 ” pins) conventionally installed. This advantage becomes more pronounced as the number of pixels increases.

Transient Thermal Mapping of Pixel Modulation

To quantitatively understand the response speed of an individual pixel on the 2D array displaying dynamic infrared patterns via pixel sweeping, thermal transient simulations are performed on a single pixel device, where transient responses of temperature change (ΔT) due to voltage modulations are collected. Such responses are then verified by the reflectivity change ($\Delta R/R$) measured via time-domain thermoreflectance temperature mapping on a fabricated single pixel device (details in the “Method” section). Here two modulation schemes are demonstrated: (1) gate-voltage modulation using a single gate voltage pulse $V_g = 4$ V with constant drain voltage $V_d = 6$ V and grounded source electrode to change the relative brightness of each pixel, and (2) source-drain-voltage on/off modulation using a single drain voltage pulse $V_d = 8$ V with constant grounded V_g to activate and deactivate each pixel row. The pulse width of both modulations is set as 7.5 μs , and the monolayer graphene is measured to have the Dirac point about $V_{Dirac} = 1.4$ V (device setup and electrical measurements in Supplementary S4). Figures 5(a) and (b) show the simulated and experimental transient response curve of the two modulations, capturing each time frame of the surface temperature and reflectivity changes by averaging the whole nanoantenna array area, as indicated by the dashed-line box in Fig. 5(c).

For the gate-voltage modulation shown in Fig. 5(a), initial $V_g = -2$ V is provided at time $t = 0$ μs . Applying boundary conditions of $V(0) = V_d$ and $V(L) = V_s$, analytical calculation (Supplementary S1) gives the Dirac point location $x_0 > L$ and electrical current $I = 8.7$ mA, indicating that the whole graphene channel is at the hole dominant region resulting in a relatively low total resistance (Fig. 5(c)). When t reaches 1.5 μs , V_g is set to 4 V. As a result, $x_0 = 0.63L$ and $I = 2.1$ mA, hence such reduced current causes a reduction of heat generation and a drop in the average temperature. The ongoing increases of reflectance difference $\Delta R/R$ with $V_g = 4$ V at $t = 2.1$ μs and $t = 6.9$ μs are captured on mapping photos in Figs. 5(d) and (e), corresponding to temperature decreases across the channel. These thermoreflectance mappings also depict the spatial temperature modulation, where the location of the Dirac point $x_0 = 0.63L$ near the source (bottom) electrode is implied by a smaller $\Delta R/R$ value and verified by simulation. Finally, at $t = 9$ μs , V_g switches back to -2 V, which brings heat generation pattern back to the initial condition. The surface temperature rises again while magnitude of $\Delta R/R$ decays, as shown by the overall

fainted red color in Fig. 5(f). In the full cycle of temperature falling and rising, the 10 to 90% fall time and rise time are measured to be $t_{f1} = 2.3 \mu\text{s}$ and $t_{r1} = 2.4 \mu\text{s}$, respectively (see Supplementary videos). Similar procedures are followed for source-drain voltage on/off modulation as shown in Fig. 5(b) where V_g and the source electrode are kept grounded, V_d is set to 0 V at $t = 0 \mu\text{s}$, up to 8 V at $t = 1.5 \mu\text{s}$, and back to 0 V at $t = 9 \mu\text{s}$. The temperature rising and falling profile and reflectivity change are captured to have satisfactory match of each other, with $t_{r2} = 1.9 \mu\text{s}$ and $t_{f2} = 2.3 \mu\text{s}$. Figures 5(g) to (j) show typical mapping photos at the same time frames as Figs. 5(c) to (f). It is worth noting that at $t = 6.9 \mu\text{s}$, Figure 5(i) depicts a hot spot near the source (bottom) electrode as an intensified blue color, which is also verified by simulation and analytical modeling (Supplementary S1). The response speed of the electrothermally driven metasurface is limited by its speed of thermal dissipation to the substrate. We apply a lumped-capacitance thermal circuit model, which is related to the 10 to 90% rise time τ_r by $f_c = 0.35/\tau_r$ ⁴³, to obtain the 3-dB cutoff frequencies for the gate-voltage modulation as $f_{c1} = 146 \text{ kHz}$ and for the source-drain-voltage on/off modulation as $f_{c2} = 184 \text{ kHz}$. The device speed can potentially reach *MHz*-level by optimizing the substrate design and the size of metasurface for heat transfer^{44,57}.

Conclusion

In summary, we demonstrate a pixelated electrically driven plasmonic metasurface integrated with the Gr-FET for dynamic coherent mid-infrared emission. The free-form design of plasmonic nanoantennas in combination with the ultrabroad infrared transparency of graphene enables tuning of different coherent states, including resonant wavelengths and polarizations. The 2D pixelated high-speed dynamics is achieved by integrating the emissivity control with the spatial temperature tuning by the Gr-FET, with the bandwidth of about 146 kHz. With the highly dynamic control of electromagnetic responses in the infrared range, our implementation of graphene-integrated active metasurfaces has important implications in infrared lab-on-a-chip, chemical and biological sensing, personalized health monitoring, and portable real-time beam shaping and steering.

References

1. Shaltout, A. M., Shalaev, V. M. & Brongersma, M. L. Spatiotemporal Light Control with Active Metasurfaces. *Science* **364**, eaat3100 (2019).
2. Gu, T., Kim, H. J., Rivero-Baleine, C. & Hu, J. Reconfigurable Metasurfaces Towards Commercial Success. *Nat. Photon.* **17**, 48–58 (2023).
3. Kwon, H., Arbabi, E., Kamali, S. M., Faraji-Dana, M. & Faraon, A. Single-Shot Quantitative Phase Gradient Microscopy Using a System of Multifunctional Metasurfaces. *Nat. Photonics* **14**, 109–114 (2020).
4. Rubin, N. A. *et al.* Matrix Fourier Optics Enables a Compact Full-Stokes Polarization Camera. *Science* **365**, eaax1839 (2019).
5. Faraji-Dana, M. *et al.* Compact Folded Metasurface Spectrometer. *Nat Commun* **9**, 4196 (2018).
6. Park, J. *et al.* All-Solid-State Spatial Light Modulator with Independent Phase and Amplitude Control for Three-Dimensional Lidar Applications. *Nat. Nanotechnol.* **16**, 69–76 (2021).
7. Li, S.-Q. *et al.* Phase-Only Transmissive Spatial Light Modulator Based on Tunable Dielectric Metasurface. *Science* **364**, 1087–1090 (2019).
8. Zheng, G. *et al.* Metasurface holograms reaching 80% efficiency. *Nature Nanotech* **10**, 308–312 (2015).
9. Li, L. *et al.* Electromagnetic reprogrammable coding-metasurface holograms. *Nat Commun* **8**, 197 (2017).
10. Fattal, D. *et al.* A multi-directional backlight for a wide-angle, glasses-free three-dimensional display. *Nature* **495**, 348–351 (2013).
11. Shalaginov, M. Y. *et al.* Design for Quality: Reconfigurable Flat Optics Based on Active Metasurfaces. *Nanophotonics* **9**, 3505–3534 (2020).
12. Colombelli, R. *et al.* Quantum Cascade Surface-Emitting Photonic Crystal Laser. *Science* **302**, 1374–1377 (2003).
13. Yao, Y., Hoffman, A. J. & Gmachl, C. F. Mid-infrared quantum cascade lasers. *Nature Photon* **6**, 432–439 (2012).
14. Zhang, Y. *et al.* Electrically Reconfigurable Non-Volatile Metasurface Using Low-Loss Optical Phase-Change Material. *Nat. Nanotechnol.* **16**, 661–666 (2021).

15. Wang, Y. *et al.* Electrical Tuning of Phase-Change Antennas and Metasurfaces. *Nat. Nanotechnol.* **16**, 667–672 (2021).
16. King, J. *et al.* Electrically tunable VO₂–metal metasurface for mid-infrared switching, limiting and nonlinear isolation. *Nat. Photon.* **18**, 74–80 (2024).
17. Abdollahramezani, S. *et al.* Electrically Driven Reprogrammable Phase-Change Metasurface Reaching 80% Efficiency. *Nat Commun* **13**, 1696 (2022).
18. Li, Y. *et al.* Transforming Heat Transfer with Thermal Metamaterials and Devices. *Nat Rev Mater* **6**, 488–507 (2021).
19. Li, W. & Fan, S. Nanophotonic Control of Thermal Radiation for Energy Applications [invited]. *Opt. Express* **26**, 15995 (2018).
20. Fan, S. Thermal Photonics and Energy Applications. *Joule* **1**, 264–273 (2017).
21. Baranov, D. G. *et al.* Nanophotonic Engineering of Far-Field Thermal Emitters. *Nat. Mater.* **18**, 920–930 (2019).
22. Overvig, A. C., Mann, S. A. & Alù, A. Thermal Metasurfaces: Complete Emission Control by Combining Local and Nonlocal Light-Matter Interactions. *Phys. Rev. X* **11**, 021050 (2021).
23. Liu, B., Gong, W., Yu, B., Li, P. & Shen, S. Perfect Thermal Emission by Nanoscale Transmission Line Resonators. *Nano Lett.* **17**, 666–672 (2017).
24. Liu, X. *et al.* Taming the Blackbody with Infrared Metamaterials as Selective Thermal Emitters. *Phys. Rev. Lett.* **107**, 045901 (2011).
25. Greffet, J.-J. *et al.* Coherent Emission of Light by Thermal Sources. *Nature* **416**, 61–64 (2002).
26. Schuller, J. A., Taubner, T. & Brongersma, M. L. Optical Antenna Thermal Emitters. *Nature Photon* **3**, 658–661 (2009).
27. Lu, G. *et al.* Narrowband Polaritonic Thermal Emitters Driven by Waste Heat. *ACS Omega* **5**, 10900–10908 (2020).
28. Guo, Y. & Fan, S. Narrowband Thermal Emission from a Uniform Tungsten Surface Critically Coupled with a Photonic Crystal Guided Resonance. *Opt. Express, OE* **24**, 29896–29907 (2016).
29. Yang, C., Cai, W. & Zhang, Z. M. Tailoring full-Stokes thermal emission from twisted-gratings structures. *Nanophotonics* (2023) doi:10.1515/nanoph-2023-0395.

30. Qu, Y. *et al.* Dynamic Thermal Emission Control Based on Ultrathin Plasmonic Metamaterials Including Phase-Changing Material GST. *Laser & Photonics Reviews* **11**, 1700091 (2017).
31. Li, Z. *et al.* Brochosome-Inspired Binary Metastructures for Pixel-by-Pixel Thermal Signature Control. *Science Advances* **10**, ead14027 (2024).
32. Liu, X. & Padilla, W. J. Reconfigurable Room Temperature Metamaterial Infrared Emitter. *Optica, OPTICA* **4**, 430–433 (2017).
33. Coppens, Z. J. & Valentine, J. G. Spatial and Temporal Modulation of Thermal Emission. *Advanced Materials* **29**, 1701275 (2017).
34. Emani, N. K. *et al.* Electrical Modulation of Fano Resonance in Plasmonic Nanostructures Using Graphene. *Nano Lett.* **14**, 78–82 (2014).
35. Yao, Y. *et al.* Wide Wavelength Tuning of Optical Antennas on Graphene with Nanosecond Response Time. *Nano Lett.* **14**, 214–219 (2014).
36. Brar, V. W. *et al.* Electronic Modulation of Infrared Radiation in Graphene Plasmonic Resonators. *Nat Commun* **6**, 7032 (2015).
37. Zeng, B. *et al.* Hybrid Graphene Metasurfaces for High-Speed Mid-Infrared Light Modulation and Single-Pixel Imaging. *Light Sci Appl* **7**, 51 (2018).
38. Kim, S. *et al.* Electronically Tunable Perfect Absorption in Graphene. *Nano Lett.* **18**, 971–979 (2018).
39. Zhao, H. *et al.* Gate-Tunable Metafilm Absorber Based on Indium Silicon Oxide. *Nanophotonics* **8**, 1803–1810 (2019).
40. Park, J., Kang, J.-H., Kim, S. J., Liu, X. & Brongersma, M. L. Dynamic Reflection Phase and Polarization Control in Metasurfaces. *Nano Lett.* **17**, 407–413 (2017).
41. Yi, F. *et al.* Voltage Tuning of Plasmonic Absorbers by Indium Tin Oxide. *Applied Physics Letters* **102**, 221102 (2013).
42. Liu, X. *et al.* Electrically Driven Thermal Infrared Metasurface with Narrowband Emission. *Applied Physics Letters* **121**, 131703 (2022).
43. Liu, X. *et al.* Direct Measurement of Electrically Modulated Far-Field Thermal Infrared Emission and its Dynamics. *Phys. Rev. Appl.* **19**, 034040 (2023).
44. Wojszwyk, L. *et al.* An Incandescent Metasurface for Quasimonochromatic Polarized Mid-Wave Infrared Emission Modulated Beyond 10 Mhz. *Nat Commun* **12**, 1492 (2021).

45. Thureja, P. *et al.* Array-Level Inverse Design of Beam Steering Active Metasurfaces. *ACS Nano* **14**, 15042–15055 (2020).
46. Shirmanesh, G. K., Sokhoyan, R., Wu, P. C. & Atwater, H. A. Electro-Optically Tunable Multifunctional Metasurfaces. *ACS Nano* **14**, 6912–6920 (2020).
47. Kim, S. I. *et al.* Two-Dimensional Beam Steering with Tunable Metasurface in Infrared Regime. *Nanophotonics* **11**, 2719–2726 (2022).
48. Galashev, A. E. & Rakhmanova, O. R. Mechanical and thermal stability of graphene and graphene-based materials. *Phys.-Usp.* **57**, 970 (2014).
49. Lee, C., Wei, X., Kysar, J. W. & Hone, J. Measurement of the Elastic Properties and Intrinsic Strength of Monolayer Graphene. *Science* **321**, 385–388 (2008).
50. Nair, R. R. *et al.* Fine Structure Constant Defines Visual Transparency of Graphene. *Science* **320**, 1308–1308 (2008).
51. Yan, H. *et al.* Infrared Spectroscopy of Wafer-Scale Graphene. *ACS Nano* **5**, 9854–9860 (2011).
52. Miyoshi, Y. *et al.* High-Speed and on-Chip Graphene Blackbody Emitters for Optical Communications by Remote Heat Transfer. *Nat Commun* **9**, 1279 (2018).
53. Kim, Y. D. *et al.* Ultrafast Graphene Light Emitters. *Nano Lett.* **18**, 934–940 (2018).
54. Bae, M.-H., Islam, S., Dorgan, V. E. & Pop, E. Scaling of High-Field Transport and Localized Heating in Graphene Transistors. *ACS Nano* **5**, 7936–7944 (2011).
55. Bae, M.-H., Ong, Z.-Y., Estrada, D. & Pop, E. Imaging, Simulation, and Electrostatic Control of Power Dissipation in Graphene Devices. *Nano Lett.* **10**, 4787–4793 (2010).
56. Freitag, M., Chiu, H.-Y., Steiner, M., Perebeinos, V. & Avouris, P. Thermal infrared emission from biased graphene. *Nature Nanotech* **5**, 497–501 (2010).
57. Liu, X., Li, Z., Wang, Z., Yun, H. S. & Shen, S. Design and Analysis of Electrothermal Metasurfaces. *Front. Energy* **17**, 134–140 (2023).

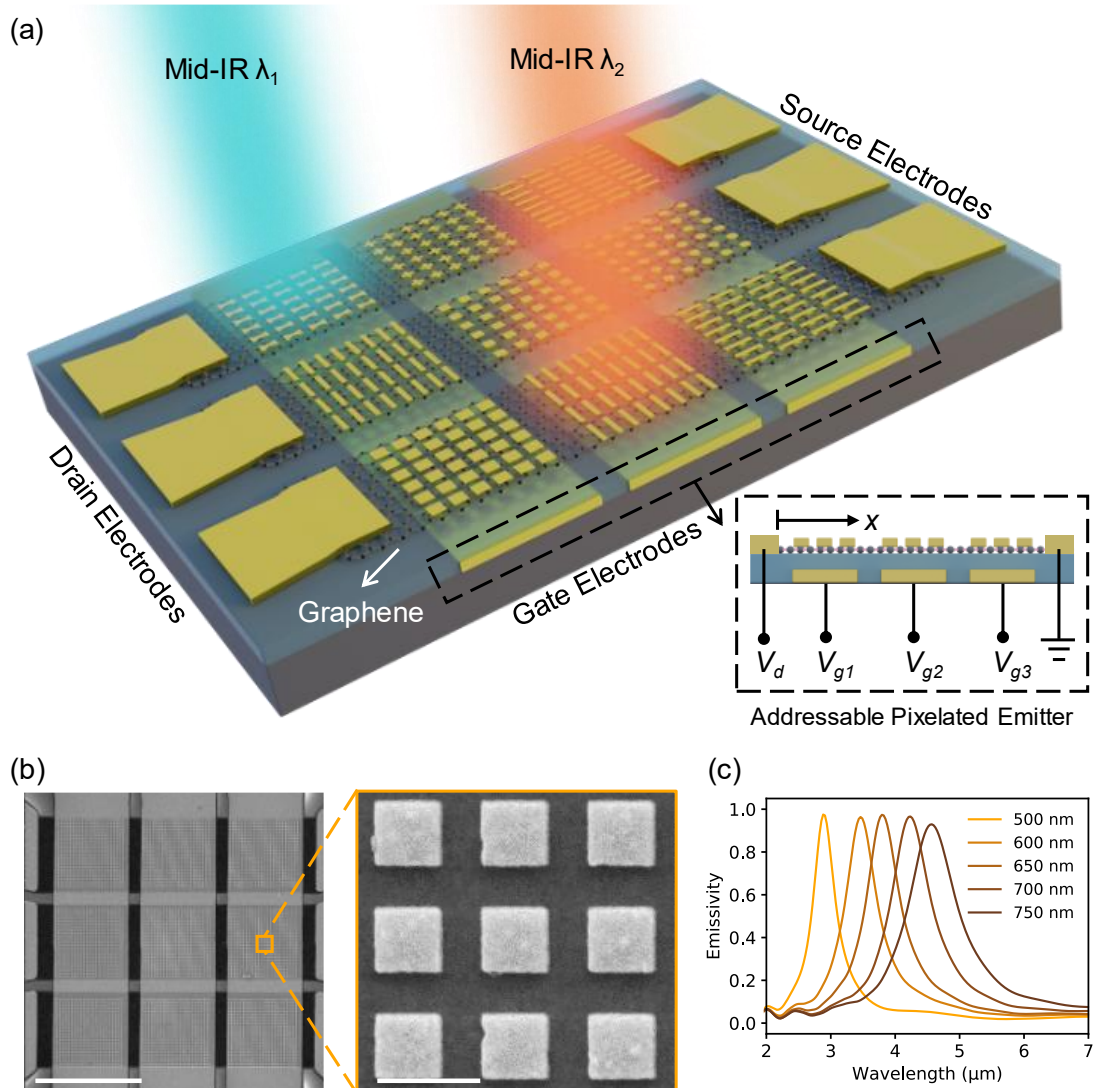


Figure 1: Mechanism of a pixelated electrical-programmable graphene-integrated plasmonic metasurface. (a) Schematic of a 3×3 pixelated MIM active metasurface driven by Gr-FETs. Each pixel contains an upper layer of an Au nanoantenna array for coherent mid-infrared emission. The beneath layers of Al_2O_3 and Au serve as the gate dielectric and spacer, and the gate electrode and mirror for the Gr-FET and MIM metasurface, respectively. Inset: Addressable pixelated mode with a patterned gate electrode assigning one gate electrode to each pixel. (b) SEM image (scale bar: $35 \mu\text{m}$) of the fabricated active metadvice with its zoom-in image (scale bar: 800 nm) revealing the nanosquare meta-atoms with an edge length of 500 nm . (c) FDTD simulations of resonant spectra as nanosquare sizes vary between 500 nm and 750 nm . The mid-infrared transparency of graphene permits free-form meta-atom designs for versatile coherent emission.

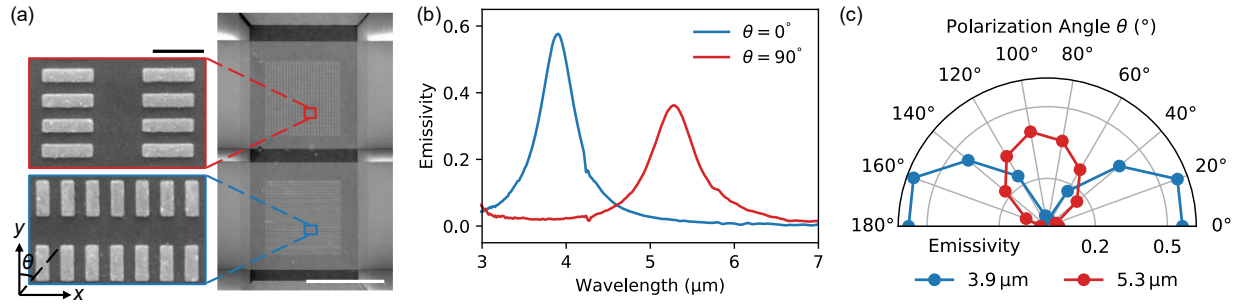


Figure 2: Experimental demonstration of single-pixel tunability for coherent emission. (a) SEM image (scale bar: 50 μm) of two pixels comprised of perpendicular Au nanorods with distinct lengths on a single graphene channel. The zoom-in images (scale bar: 1 μm) illustrate the upper pixel (red rectangle) with a longitudinal edge of 1 μm along the x -axis and the lower pixel (blue rectangle) with a longitudinal edge of 700 nm along the y -axis. (b) Emissivity spectra of the upper pixel at 5.3 μm (red line) with a polarization angle of $\theta = 90^\circ$ and the lower pixel at 3.9 μm (blue line) with $\theta = 0^\circ$. (c) Polar plots of the emissivity peaks across the polarization angles from 0° to 180° . Two distinct orthogonal polarization states are evident for the two pixels.

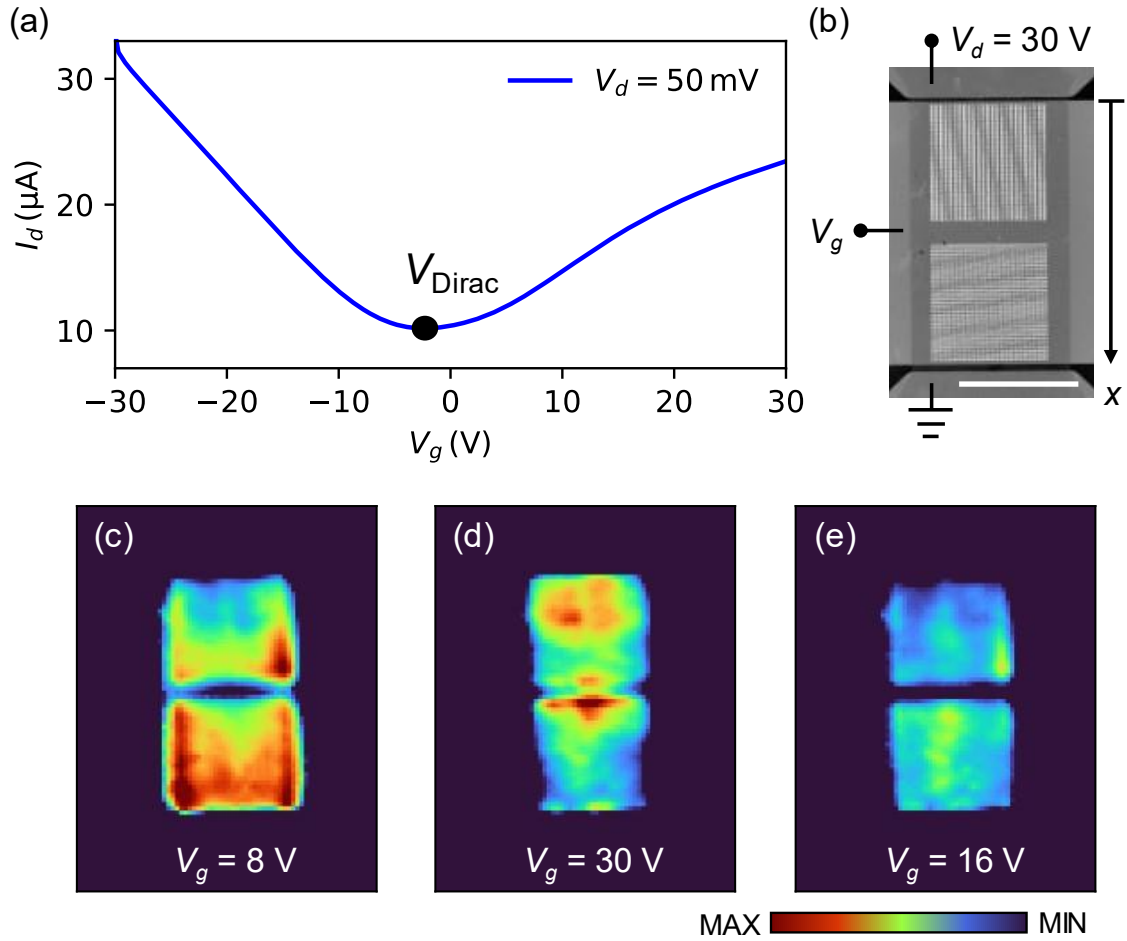


Figure 3: Experimental demonstration of spatial temperature modulation of a Gr-FET. (a) Preliminary sweep of drain current versus gate voltage $I_d - V_g$ under a drain voltage $V_d = 50 \text{ mV}$, where the source electrode is grounded. The low V_d confirms almost equal potential between the source and drain electrodes, allowing the determination of the Dirac voltage $V_{\text{Dirac}} = -2 \text{ V}$ for the Gr-FET. (b-e) Continuous spatial temperature modulation under $V_d = 30 \text{ V}$. The SEM image (scale bar: $50 \mu\text{m}$) shows two pixels with the same resonant emissivity on a single bottom gate electrode. Thermal mapping images exhibit the hot spot control by aligning V_g .

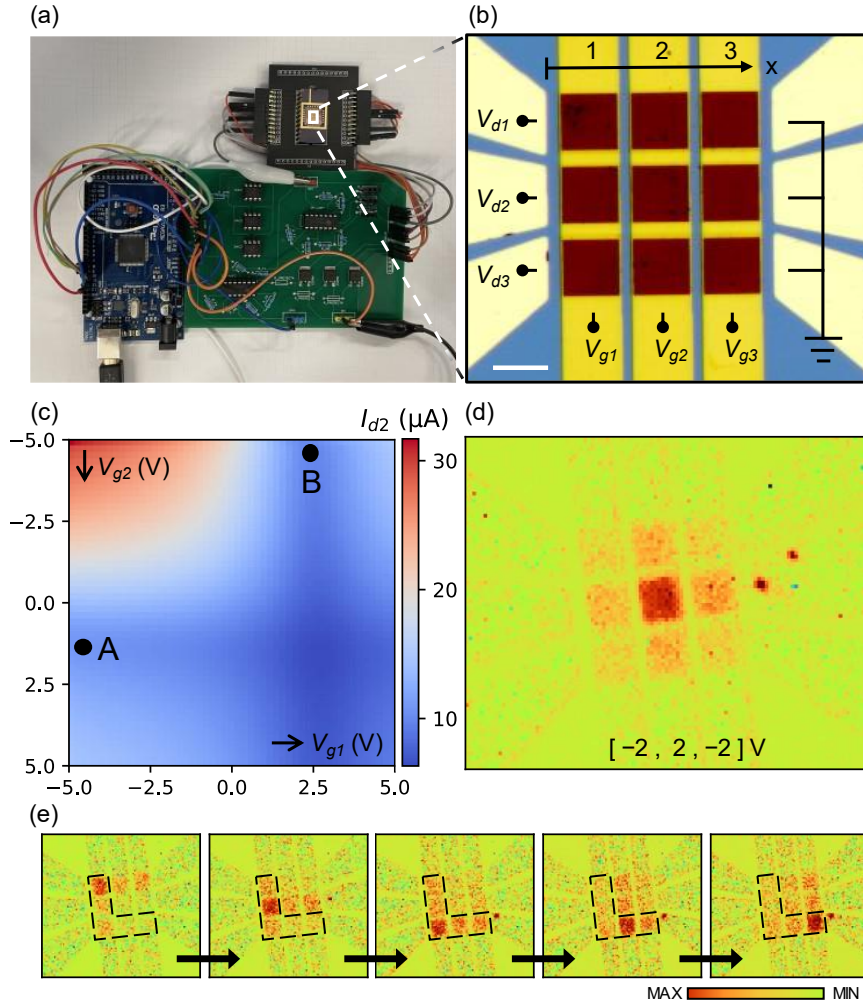


Figure 4: Experimental demonstration of the addressable pixelated mode for a 2D array display. (a) Picture of the custom-designed PCB-integrated active metasurface system. (b) Magnified image (scale bar: $25 \mu\text{m}$) of the 3×3 pixelated 2D metasurface array, accompanied by a schematic depiction of wire bonding. (c) Sweep mapping of $I_{d2} - (V_{g1}, V_{g2})$ under $V_{d2} = 50 \text{ mV}$ where the 3rd gate is grounded. For each V_{g1} value, sweeping $I_{d2} - V_{g2}$ maintains the bipolar transport curve of the Gr-FET. Tuning V_{g2} enables control over the V_{Dirac} alignment for pixel on/off. Setting apart from V_{Dirac} (Point A) boosts the overall current for pixel brightness. Symmetrically, this approach applies to $I_{d2} - V_{g1}$ sweep under V_{g2} control, represented by Point B. (d) Thermal mapping images under three gate voltages $[V_{g1}, V_{g2}, V_{g3}]$ in $[-2, 2, -2]$ V. The discrete adjustment of gate electrodes under $V_d = 5 \text{ V}$ results in pixel resistances $[R_1, R_2, R_3] = [529, 1877, 1023] \Omega$ lighting up the central pixel. (e) Thermal mapping of individual frames displaying the letter "L".

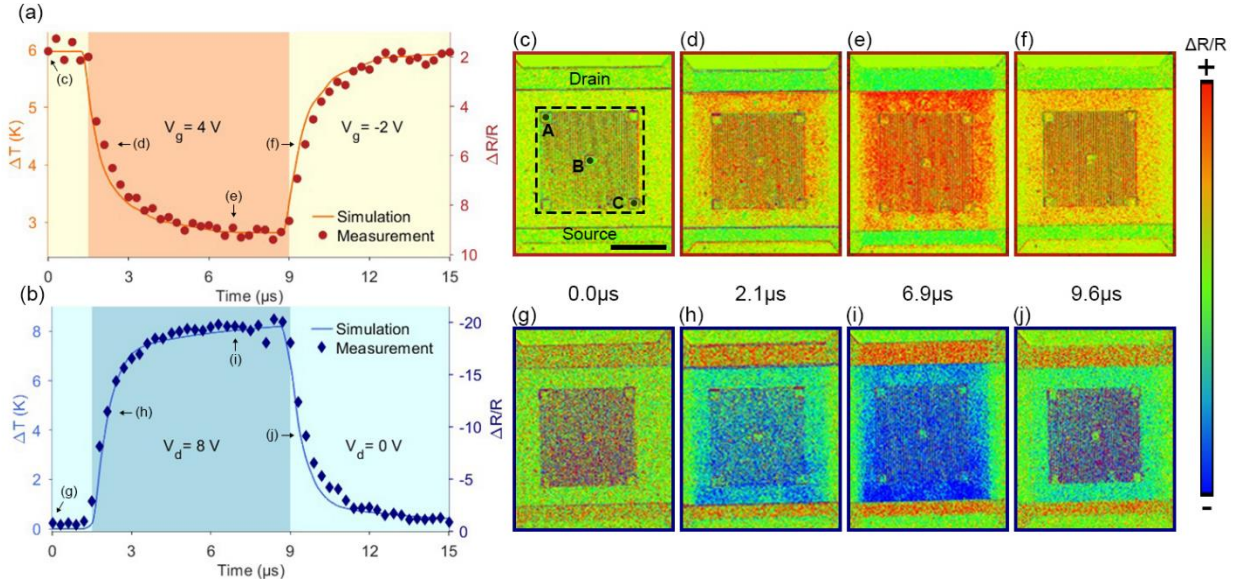


Figure 5: Simulation and experiment of transient single-pixel modulation. (a) Gate-voltage modulation with respective thermoreflectance mapping frames at $t = [0, 2.1, 6.9, 9.6] \mu s$ shown in (c) to (f) (scale bar: $25 \mu m$). The upper electrode is the drain electrode, and the lower electrode is the source electrode. Five enlarged Au pads are deposited at the four corners and the center of the array, acting as transducers for the local reflectance measurement and alignment. Local reflectance measurements of three labeled pads A, B and C are given in Supplementary S5. (b) Source-drain-voltage on/off modulation with respective thermoreflectance mapping frames at $t = [0, 2.1, 6.9, 9.6] \mu s$ shown in (g) to (j). The gate-voltage modulation shows a cutoff frequency $f_{c1} = 146$ kHz, while the source-drain-voltage on/off modulation has its cutoff frequency $f_{c2} = 184$ kHz.

Methods

Device fabrication

Monolayer graphene is synthesized via low-pressure chemical vapor deposition (LPCVD) on a 99.9% pure Cu foil. The Cu foil is polished via electrochemical polishing in 85% phosphoric acid for 2.5 hours. It is then cleaned by deionized water and moved into an LPCVD quartz tube furnace. 4-hour hydrogen annealing is performed with 140 standard-cubic-centimeter per minute (sccm) hydrogen flow until a pressure of 4 torr is stabilized. 3 sccm methane and 137 sccm hydrogen mixing gas is then used to grow monolayer graphene on the Cu substrate for 30 minutes, while the pressure is kept the same. Finally, the furnace is opened for a rapid cooling with 140 sccm hydrogen gas purging until room temperature is reached.

The Gr-FET is fabricated on a Si/1 μ m-SiO₂ wafer diced into 9 mm \times 9 mm chips. The bottom gate electrodes are patterned using lift-off method: firstly, photolithography is performed with AZ P4110 photoresist; then the gate metal is deposited via e-beam evaporation of 50 nm thick Au with 2 nm Ti adhesion layer; lastly, Microposit remover 1165 is used to remove the photoresist. A 20 nm or 100 nm thick Al₂O₃ layer is deposited via thermal atomic-layer deposition (ALD) under 250 °C. The CVD-synthesized monolayer graphene is transferred using the PMMA-assisted wet transfer method and patterned to a desired shape via reactive-ion etching (RIE). The source and drain electrodes are patterned using the same method as the gate electrodes. Au metasurfaces with various thicknesses are patterned on top of the graphene layer via e-beam lithography using PMMA as the e-beam resist followed by e-beam evaporation of Au with a 2 nm Ti adhesion layer.

Thermal and optical simulation

The transient electrothermal simulation is conducted via time-domain finite-element analysis in COMSOL Multiphysics. The single pixel Gr-FET device in Fig. 5 is reconstructed in a COMSOL model, with the constant temperature boundary condition applied to the bottom surface of the simulated device. The electrical properties and setups of graphene applied in simulation are obtained from experimental designs and measurements in Supplementary Information. Material properties of Si, SiO₂, Au and Al₂O₃ are obtained from COMSOL material database.

The optical simulation is based on the Ansys Lumerical FDTD. A single period of the MIM metasurface is illuminated by a plane wave source with periodic boundary conditions. A reflective

power monitor is placed above the source to capture the reflective energy, which provides information about the emissivity based on Kirchhoff's law, revealing coherent features of the thermal infrared emission.

Spectroscopy and thermal mapping measurements

All the spectra are measured by the ThermoFisher Nicolet iS50 Fourier transform infrared spectrometer. A microscope with an adjustable aperture focuses infrared illumination on the active area of the MIM metasurface. The reflectivity is measured under different polarization angles based on a polarization filter. The current-voltage sweeps are measured by the Keysight A1500A semiconductor device analyzer. The custom-designed PCB testing system consists of software codes and control circuits. During testing, control commands (codes) are first compiled by Arduino software and then sent to an ATmega-2560 micro-controller unit (MCU) development board. For the gate control, 16 bits digital signals/data are sent to 3 digital-to-analog converters (DACs) that are simply made by digital potential meters, respectively, from the MCU. Then, 3 OPAMP amplifiers map the $0 \sim 5V$ analog voltages from the DACs to $-5 \sim 5V$ gate control. For graphene device source and drain controls, each of its source pads is connected to an N-MOSFET. By wiring an output port of the MCU to the gate of the N-MOSFET, each source and drain can be turned on or off individually. The static and dynamic thermal mapping images are then captured by the QFI InfraScope system. In the time-domain thermoreflectance measurements, a 530-nm monochrome incident LED lights up the pixel area before being reflected and captured by a CCD camera. The reflectivity change is linearly proportional to the surface temperature change: $\Delta R/R = C_{TR}\Delta T$, where C_{TR} is the thermoreflectance coefficient depending on surface material and beam wavelength. Au has a local minimum of negative C_{TR} under 530-nm incident wavelength, hence $\Delta R/R$ will decrease with increase of temperature change, and vis versa.

Acknowledgements

This work is funded by the National Science Foundation (Grant No. CBET-1931964) and Defense Threat Reduction Agency (Grant No. HDTRA1-19-1-0028). H.Z.W., Z.E.W., and J. K. acknowledge the support from the Semiconductor Research Corporation Center 7 in JUMP 2.0 (Grant No. 145105-21913) and the U.S. Army DEVCOM ARL Army Research Office through the

MIT Institute for Soldier Nanotechnologies under Cooperative Agreement number W911NF-23-2-0121.

Author Contributions

S.S., X.Z., and X.L. conceived the project, with S.S. and X.Z. providing the overall supervision. X.L. and Y.B.Z. led the device design and optimization. The optical simulations were conducted by X.L. and the electrothermal simulations were done by Y.B.Z. and Z.X.W. The graphene layers were grown and transferred by Y.B.Z., J.Y.Z., H.Z.W., Z.E.W., and J.K., and metasurface fabrication was finished by X.L., Y.B.Z., and S.L., with inputs from Z.X.W. The experimental setup and characterization were undertaken by X.L., Y.B.Z., and T.Y.H. The data analysis was led by X.L., Y.B.Z., S.S., and X.Z., with contributions from all co-authors. The manuscript was written by X.L., Y.B.Z., and S.S., with contributions from all co-authors.

Competing Interests

The authors declare no competing interests.

Supplementary Information to “Electrically Programmable Pixelated Graphene-Integrated Plasmonic Metasurfaces for Coherent Mid-Infrared Emission”

Xiu Liu^{1,†}, Yibai Zhong^{1,†}, Zexiao Wang¹, Tianyi Huang¹, Sen Lin², Jingyi Zou², Haozhe Wang⁴, Zhiem Wang⁴, Zhuo Li¹, Xiao Luo¹, Rui Cheng¹, Jiayu Li¹, Hyeong Seok Yun¹, Han Wang³, Jing Kong⁴, Xu Zhang^{2,}, Sheng Shen^{1,*}*

¹*Department of Mechanical Engineering, Carnegie Mellon University, Pittsburgh, PA, USA*

²*Department of Electrical and Computer Engineering, Carnegie Mellon University, Pittsburgh, PA, USA*

³*Department of Electrical and Electronic Engineering, University of Hong Kong, Hong Kong, China*

⁴*Department of Electrical Engineering and Computer Science, Massachusetts Institute of Technology, Cambridge, MA, USA*

*(† denotes equal contribution, * denotes corresponding authors)*

S1: Figures S1-1 (a) and (b) illustrate the operational principles of the active metasurface functioning at single-pixel and multiple-pixel modes.

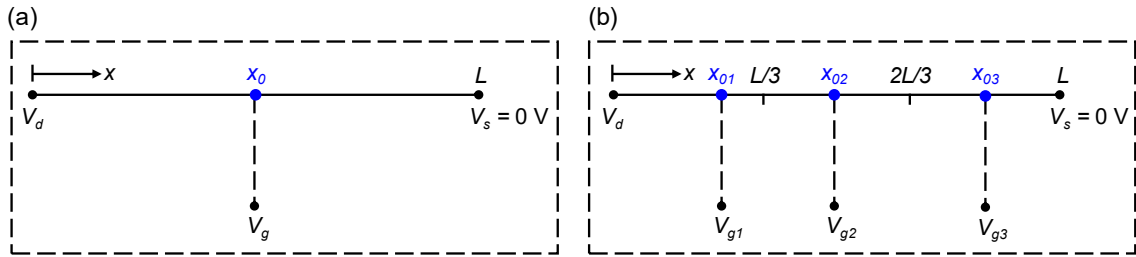


Figure S1-1: Mechanism schematics of spatial temperature modulation for (a) continuous (1-pixel) and (b) addressable pixelated (3-pixel).

At a given drain voltage V_d with the sourced grounded ($V_s = 0 V$), a steady current

$$I = W\mu en(x) \left[-\frac{dV(x)}{dx} \right] \quad (s1)$$

is constant along the graphene channel, where W is the width of graphene channel, μ is the carrier mobility that is approximated as constant¹⁻⁴, e is the electron charge, $n(x)$ is the local carrier density per unit area, and $V(x)$ is the local electric potential. Then the Joule heating power $P(x) = I[dV(x)/dx]$ reaches its maximum at the position where the intensity of local electric field $dV(x)/dx$ is highest, coinciding with the location of the lowest $n(x)$. Simultaneously, the local gate voltage $V_{g,local}(x)$ controls the local charge density per unit area $\rho_e(x)$ by

$$V_{Dirac} - V_{g,local}(x) = V_{Dirac} - [V_g - V(x)] = \frac{1}{C_{ox}} \rho_e(x) \quad (s2)$$

following the Gr-FET bipolar transport characteristics, where V_g is the gate voltage and C_{ox} is the gate dielectric capacitance per unit area. V_{Dirac} is the Dirac voltage corresponding to the neutrality point of graphene depending on its intrinsic doping and substrate. Under a negligible source-drain bias ($V_d \approx 0$ V), the graphene channel can be approximated as equipotential with $V(x) = 0$ V, and we can measure $V_{Dirac} = V_g$ corresponding to the minimal $\rho_e(x)$.

We assume a negligible recombination length so at any x there are holes or electrons but not both¹⁻⁴, the constraints of Eq. (s1) and (s2) on the local voltage $V(x)$ can be connected by

$$\rho_e(x) = \begin{cases} n(x)e, & x \leq x_0 \\ -n(x)e, & x_0 \leq x \end{cases} \quad (s3)$$

where $x \leq x_0$ is the hole region with $V_{Dirac} - V_{g,local}(x) > 0$ and $x_0 \leq x$ is the electron region with $V_{Dirac} - V_{g,local}(x) < 0$. Summarizing the sign convention, we have

$$n(x) = -\frac{\text{sgn}(x - x_0)\rho_e(x)}{e} \quad (s4)$$

$$V_{Dirac} - V_{g,local}(x) = -\text{sgn}(x - x_0)|V_{Dirac} - [V_g - V(x)]| \quad (s5)$$

Input Eq. (s2) into (s1) for

$$I = \text{sgn}(x - x_0) \mu W C_{ox} \{-\text{sgn}(x - x_0)|V_{Dirac} - [V_g - V(x)]|\} \frac{dV(x)}{dx} \quad (s6)$$

with 3 boundary conditions: (a) at $x = x_0$, $V_{Dirac} - [V_g - V(x_0)] = 0$, (b) at $x = 0$, $V(0) = V_d$, (c) at $x = L$, $V(L) = 0$ V, where L is the length of the graphene channel, we have

$$V_{Dirac} - [V_g - V(x)] = -\text{sgn}(x - x_0) \sqrt{\text{sgn}(x - x_0) C(x - x_0)}, \quad 0 \leq x \leq L \quad (s7)$$

$$V_{Dirac} - [V_g - V_d] = -\text{sgn}(0 - x_0) \sqrt{\text{sgn}(0 - x_0) C(0 - x_0)} \quad (s8)$$

$$V_{Dirac} - [V_g - 0] = -\text{sgn}(L - x_0) \sqrt{\text{sgn}(L - x_0) C(L - x_0)} \quad (s9)$$

where $C = 2I/\mu W C_{ox}$. Thus, we can find the Dirac point x_0 by

$$\frac{\text{sgn}(x_0 - L)}{\text{sgn}(x_0)} \sqrt{\frac{\text{sgn}(L - x_0) (L - x_0)}{\text{sgn}(-x_0) (-x_0)}} = \frac{V_{Dirac} - V_g}{V_{Dirac} - V_g + V_d} \quad (s10)$$

and the current I from the constant C .

The local resistivity $\rho(x)$ can be obtained by inputting $V(x)$ as

$$\rho(x) = \frac{1}{\mu e n(x)} = \sqrt{\frac{W}{2I C_{ox} \mu}} \frac{1}{\sqrt{\text{sgn}(x - x_0)(x - x_0)}} \quad (s11)$$

Based on the sign conventions (s4) and (s5), the above formulas have already included the cases for x_0 outside $[0, L]$. If $x_0 < 0$, i.e., the whole $[0, L]$ is in electron region, the maximum of $\rho(x)$ is at the source side. If $x_0 > L$, i.e., the whole $[0, L]$ is in hole region, the maximum of $\rho(x)$ is at the drain side.

The 3-pixel case can be regarded as 3 Gr-FETs in series. With the boundary conditions: (i) at $x = x_{01}$, $V_{Dirac} - [V_{g1} - V(x)] = 0$, (ii) at $x = x_{02}$, $V_{Dirac} - [V_{g2} - V(x)] = 0$, (iii) at $x = x_{03}$, $V_{Dirac} - [V_{g3} - V(x)] = 0$, we have

$$V_{Dirac} - [V_{g1} - V(x)] = -\text{sgn}(x - x_{01}) \sqrt{\text{sgn}(x - x_{01}) C(x - x_{01})}, \quad 0 \leq x \leq \frac{L}{3} \quad (s12)$$

$$V_{Dirac} - [V_{g2} - V(x)] = -\text{sgn}(x - x_{02}) \sqrt{\text{sgn}(x - x_{02}) C(x - x_{02})}, \quad \frac{L}{3} \leq x \leq \frac{2L}{3} \quad (s13)$$

$$V_{Dirac} - [V_{g3} - V(x)] = -\text{sgn}(x - x_{03}) \sqrt{\text{sgn}(x - x_{03}) C(x - x_{03})}, \quad \frac{2L}{3} \leq x \leq L \quad (s14)$$

The other boundary conditions: (iv) At $x = L/3$, $V(L/3)$ is continuous. (v) at $x = 2L/3$, $V(2L/3)$ is continuous. (vi) at $x = 0$, $V(0) = V_d$, (vii) at $x = L$, $V(L) = 0$ V then give

$$V_{Dirac} - \left[V_{g1} - V\left(\frac{L}{3}\right) \right] = -\operatorname{sgn}\left(\frac{L}{3} - x_{01}\right) \sqrt{\operatorname{sgn}\left(\frac{L}{3} - x_{01}\right) C\left(\frac{L}{3} - x_{01}\right)} \quad (\text{s15})$$

$$V_{Dirac} - \left[V_{g2} - V\left(\frac{L}{3}\right) \right] = -\operatorname{sgn}\left(\frac{L}{3} - x_{02}\right) \sqrt{\operatorname{sgn}\left(\frac{L}{3} - x_{02}\right) C\left(\frac{L}{3} - x_{02}\right)} \quad (\text{s16})$$

$$V_{Dirac} - \left[V_{g2} - V\left(\frac{2L}{3}\right) \right] = -\operatorname{sgn}\left(\frac{2L}{3} - x_{02}\right) \sqrt{\operatorname{sgn}\left(\frac{2L}{3} - x_{02}\right) C\left(\frac{2L}{3} - x_{02}\right)} \quad (\text{s17})$$

$$V_{Dirac} - \left[V_{g3} - V\left(\frac{2L}{3}\right) \right] = -\operatorname{sgn}\left(\frac{2L}{3} - x_{03}\right) \sqrt{\operatorname{sgn}\left(\frac{2L}{3} - x_{03}\right) C\left(\frac{2L}{3} - x_{03}\right)} \quad (\text{s18})$$

$$V_{Dirac} - [V_{g1} - V_d] = -\operatorname{sgn}(0 - x_{01}) \sqrt{\operatorname{sgn}(0 - x_{01}) C(0 - x_{01})} \quad (\text{s19})$$

$$V_{Dirac} - [V_{g3} - 0] = -\operatorname{sgn}(L - x_{03}) \sqrt{\operatorname{sgn}(L - x_{03}) C(L - x_{03})} \quad (\text{s20})$$

Thus, we can find the Dirac points x_{01}, x_{02}, x_{03} for each pixel by

$$V_{g1} - V_{g2} = -\operatorname{sgn}\left(\frac{L}{3} - x_{02}\right) \sqrt{\operatorname{sgn}\left(\frac{L}{3} - x_{02}\right) C\left(\frac{L}{3} - x_{02}\right)} + \operatorname{sgn}\left(\frac{L}{3} - x_{01}\right) \sqrt{\operatorname{sgn}\left(\frac{L}{3} - x_{01}\right) C\left(\frac{L}{3} - x_{01}\right)} \quad (\text{s21})$$

$$V_{g2} - V_{g3} = -\operatorname{sgn}\left(\frac{2L}{3} - x_{03}\right) \sqrt{\operatorname{sgn}\left(\frac{2L}{3} - x_{03}\right) C\left(\frac{2L}{3} - x_{03}\right)} + \operatorname{sgn}\left(\frac{2L}{3} - x_{02}\right) \sqrt{\operatorname{sgn}\left(\frac{2L}{3} - x_{02}\right) C\left(\frac{2L}{3} - x_{02}\right)} \quad (\text{s22})$$

$$V_{Dirac} - [V_{g1} - V_d] = -\operatorname{sgn}(0 - x_{01}) \sqrt{\operatorname{sgn}(0 - x_{01}) C(0 - x_{01})} \quad (\text{s23})$$

$$V_{Dirac} - [V_{g3} - 0] = -\operatorname{sgn}(L - x_{03}) \sqrt{\operatorname{sgn}(L - x_{03}) C(L - x_{03})} \quad (\text{s24})$$

and I again from C .

Then $\rho(x)$ can be obtained by inputting $V(x)$ as

$$\rho(x) = \sqrt{\frac{W}{2IC_{ox}\mu}} \cdot \frac{1}{\sqrt{\operatorname{sgn}(x - x_{01}) \cdot (x - x_{01})}}, \quad 0 \leq x \leq \frac{L}{3} \quad (\text{s25})$$

$$\rho(x) = \sqrt{\frac{W}{2IC_{ox}\mu}} \cdot \frac{1}{\sqrt{\operatorname{sgn}(x - x_{02}) \cdot (x - x_{02})}}, \quad \frac{L}{3} \leq x \leq \frac{2L}{3} \quad (\text{s26})$$

$$\rho(x) = \sqrt{\frac{W}{2IC_{ox}\mu}} \cdot \frac{1}{\sqrt{\text{sgn}(x - x_{03}) \cdot (x - x_{03})}}, \quad \frac{2L}{3} \leq x \leq L \quad (\text{s27})$$

The equations for x_{01} , x_{02} , x_{03} , and for I can be computed numerically by iteration. Based on these values, $\rho(x)$ can be obtained guiding the spatial temperature modulation.

S2: The MIM metasurface, composed of nanosquare meta-atoms shown in Fig. 1 (b) in the main text, is measured by the FTIR for its emissivity spectrum, revealing a resonance at 2.9 μm . As shown in Fig. S2-1, the results align closely with the FDTD simulation, with slight variation attributed to fabrication imperfections and material growth.

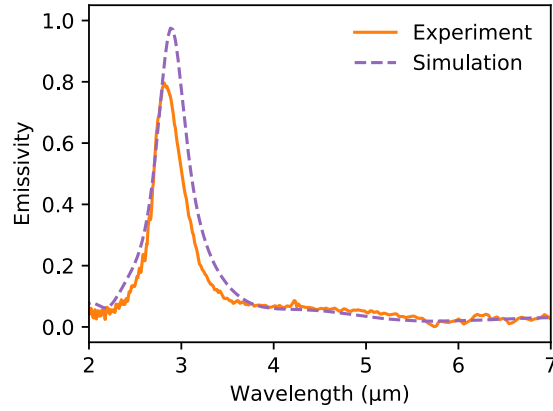


Figure S2-1: The FTIR measured and FDTD simulated spectra of the MIM metasurface shown in Fig. 1 (b) in the main text.

S3: The active metasurface device setup is shown in Fig. S3-1 (a) with a zoom-in SEM image showing the nanorod meta-atoms, corresponding to an emissivity resonance of 9.7 μm . The $I_d \sim V_g$ measurement in Fig. S3-1 (b) indicates that the Dirac voltage for the device is 16 V.

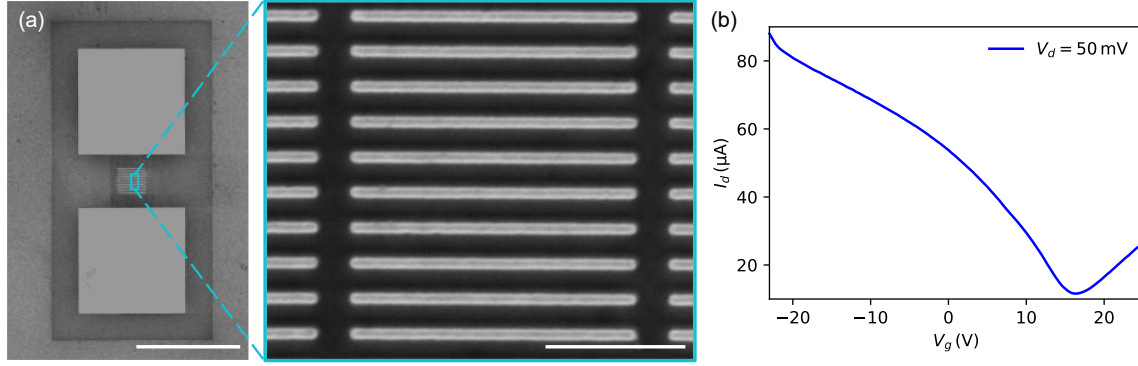


Figure S3-1: (a) SEM image (scale bar: 200 μm) of the metasurface with its zoom-in image (scale bar: 2 μm). (b) The source-drain current versus gate voltage $I_d \sim V_g$ under a drain voltage as $V_d = 50$ mV where the source is grounded.

The direct contact between the Au nanoantennas and graphene enables tunable LSPPs on the active metasurface through an electrostatic gating, where the gating-induced carrier doping in graphene alters the dielectric environment for the LSPPs from the Au nanoantennas. In Fig. S3-2, the resonance peak of the metasurface undergoes a ~ 0.5 μm blue shift beginning from a gate voltage $V_g = 16$ V (reaching the Dirac point of the graphene sample) to $V_g = -20$ V (considerably far from the Dirac point). However, pushing V_g to -23 V causes the resonance shift to saturate due to the limited carrier mobility of the CVD graphene^{5–10}.

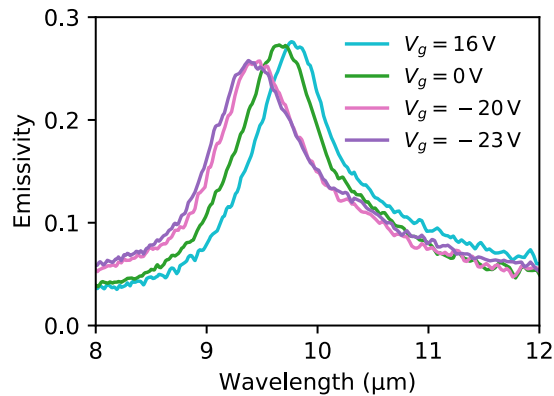


Figure S3-2: Emissivity spectra revealing a blue shift of about 0.5 μm caused by electrostatic gating from $V_g = 16$ V to $V_g = -23$ V. This emissivity shift is due to gating-induced carrier doping in graphene altering the dielectric environment for the LSPPs from the Au nanoantennas.

We demonstrate the gating induced tunability of emissivity can be coupled with the spatial temperature modulation by the Gr-FET for the coherent emission of the active metasurface. For the metasurface shown in Fig. S3-1, electrostatic gating enables tuning of the emissivity spectrum $\epsilon(\lambda)$ by modifying the dielectric environment for LSPP from the gold nanoantennas through gating-induced carrier doping in graphene. In Fig. S3-3 (a), a distinct resonance shift of emissivity is evident as the gate voltage V_g transitions from 16 V (near the Dirac point) to 0 V (far from the Dirac point) under a negligible drain voltage $V_d = 50$ mV. As V_d rises to 9.5 V, the local gate voltages $V_{g,local}(x)$ for the active metasurface under $V_g = 20$ V exhibit approximately 11.7 V near the drain edge ($x = 0.25L$) and about 18.1 V near the source edge ($x = 0.75L$). These calculations are detailed in S1 where x is the distance from the drain to the source and L is the total length of the graphene ribbon. As the metasurface aligns with the Dirac point $x = 0.65L$, we approximate its emissivity spectrum akin to $V_g = 16$ V at $V_d = 50$ mV. Likewise, at $V_g = 4$ V and $V_d = 9.5$ V, the emissivity spectrum mirrors that of $V_g = 0$ V at $V_d = 50$ mV. Simultaneously, the Joule heating by $V_d = 9.5$ V also notably changes due to the resistance change by V_g . In Fig. S3-3 (b), thermal mappings depict temperatures of $T = 46.5$ °C for $V_g = 20$ V and $T = 56.3$ °C for $V_g = 4$ V. The higher temperature for $V_g = 4$ V is due to the smaller total resistance with a fixed source-drain voltage. Thus, we can obtain their emission spectra as products of the emissivity and the Planck spectrum $I(\lambda) = \epsilon(\lambda) \cdot I_{BB}(\lambda, T)$, demonstrating the final emission contrast in Fig. S3-3 (c).

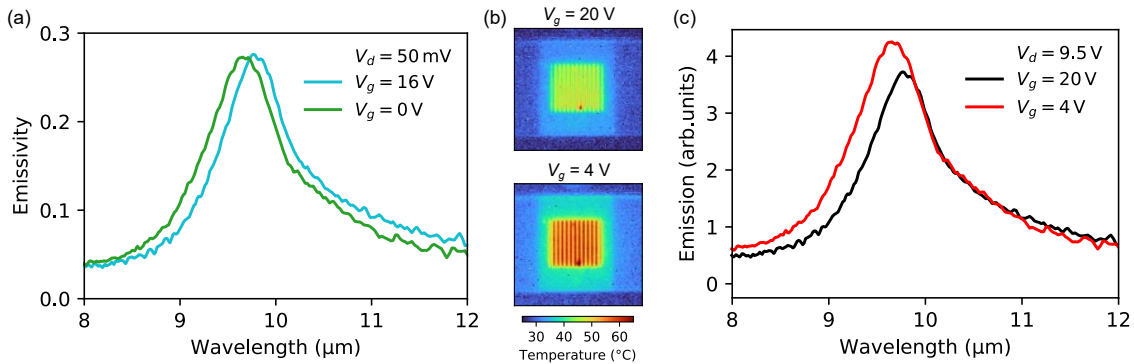


Figure S3-3: Coupled temperature-emissivity modulation. (a) Emissivity spectra of the gate voltage $V_g = 16 V$ and of $V_g = 0 V$ under the drain voltage $V_d = 50 mV$ where the source is grounded. (b) Temperature distributions and (c) emission spectra of the gate voltage $V_g = 20 V$ and of $V_g = 4 V$ under the drain voltage $V_d = 9.5 V$ where the source is grounded.

S4: The field-effect mobility of graphene is calculated from electrical measurements shown in Fig. S4-1 (b) with equation¹¹

$$\mu = \left(\frac{L}{W} \cdot \frac{1}{C'_{ox}} \cdot \frac{1}{V_d} \right) \frac{dI_d}{dV_g} \quad (s28)$$

where L and W are the channel length and width of the Gr-FET; C_{ox} is the capacitance of the gate oxide per unit area; V_d and I_d are the source-drain voltage and current of the graphene channel, respectively; and V_g represents the gate voltage of Gr-FET. For the single-pixel and multi-pixel FET devices used, $C_{ox} \approx 0.004 F/m^2$ and μ is calculated to be $731 \text{ cm}^2 V^{-1} s^{-1}$.

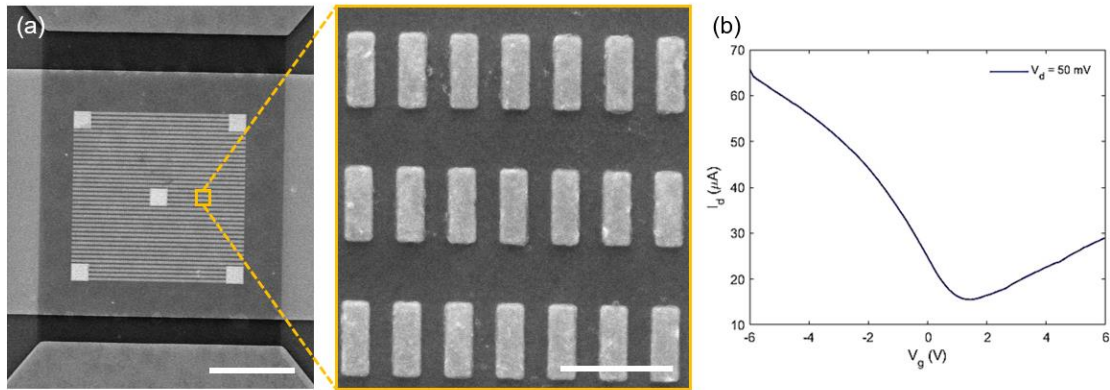


Figure S4-1: (a) SEM image (scale bar: $25 \mu m$) of the metasurface with its zoom-in image (scale bar: $1 \mu m$). (b) The source-drain current versus gate voltage $I_d \sim V_g$ under a drain voltage as $V_d = 50 \text{ mV}$ where the source is grounded.

S5:

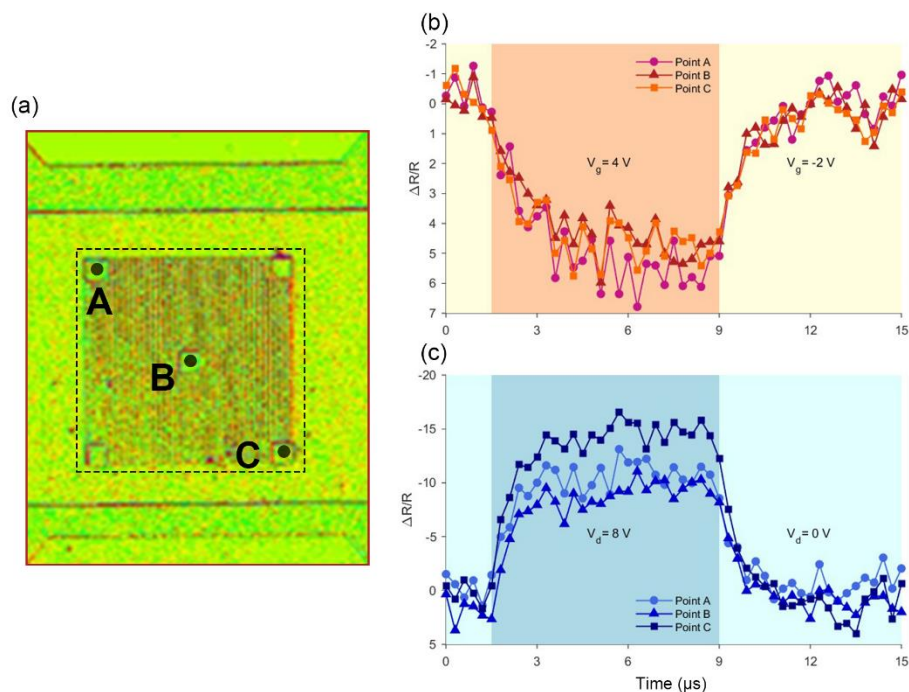


Figure S5-1: Local thermorefectance measurement for transient analysis. (a) Thermorefectance mapping frame showing location of interest as point A, B and C as shown in Fig. 5 (c) in the main text. Respective thermorefectance measurements under (b) gate-voltage modulation and (c) source-drain-voltage on/off modulation are plotted with time.

References

1. Freitag, M., Chiu, H.-Y., Steiner, M., Perebeinos, V. & Avouris, P. Thermal infrared emission from biased graphene. *Nature Nanotech* **5**, 497–501 (2010).
2. Bae, M.-H., Islam, S., Dorgan, V. E. & Pop, E. Scaling of High-Field Transport and Localized Heating in Graphene Transistors. *ACS Nano* **5**, 7936–7944 (2011).
3. Bae, M.-H., Ong, Z.-Y., Estrada, D. & Pop, E. Imaging, Simulation, and Electrostatic Control of Power Dissipation in Graphene Devices. *Nano Lett.* **10**, 4787–4793 (2010).
4. Fan, Y. *et al.* Regulation of Thermal Emission Position in Biased Graphene. *Nanomaterials* **12**, 3457 (2022).
5. Yao, Y. *et al.* Wide Wavelength Tuning of Optical Antennas on Graphene with Nanosecond Response Time. *Nano Lett.* **14**, 214–219 (2014).

6. Brar, V. W. *et al.* Electronic Modulation of Infrared Radiation in Graphene Plasmonic Resonators. *Nat Commun* **6**, 7032 (2015).
7. Zeng, B. *et al.* Hybrid Graphene Metasurfaces for High-Speed Mid-Infrared Light Modulation and Single-Pixel Imaging. *Light Sci Appl* **7**, 51 (2018).
8. Yao, Y. *et al.* Broad Electrical Tuning of Graphene-Loaded Plasmonic Antennas. *Nano Lett.* **13**, 1257–1264 (2013).
9. Kim, S. *et al.* Electronically Tunable Perfect Absorption in Graphene. *Nano Lett.* **18**, 971–979 (2018).
10. Emani, N. K. *et al.* Electrical Modulation of Fano Resonance in Plasmonic Nanostructures Using Graphene. *Nano Lett.* **14**, 78–82 (2014).
11. Leong, W. S. *et al.* Paraffin-enabled graphene transfer. *Nat Commun* **10**, 867 (2019).